

In vitro cytotoxic efficacy of PEG encapsulated manganese-doped zinc oxide nanoparticles on hepatocellular carcinoma cells

G. Vijayakumar, G. Boopathi & M. Elango

To cite this article: G. Vijayakumar, G. Boopathi & M. Elango (2019): In vitro cytotoxic efficacy of PEG encapsulated manganese-doped zinc oxide nanoparticles on hepatocellular carcinoma cells, *Materials Technology*, DOI: [10.1080/10667857.2019.1633787](https://doi.org/10.1080/10667857.2019.1633787)

To link to this article: <https://doi.org/10.1080/10667857.2019.1633787>



Published online: 27 Jun 2019.



Submit your article to this journal [↗](#)



Article views: 1



View Crossmark data [↗](#)



In vitro cytotoxic efficacy of PEG encapsulated manganese-doped zinc oxide nanoparticles on hepatocellular carcinoma cells

G. Vijayakumar, G. Boopathi and M. Elango

Department of Physics, PSG College of Arts & Science, Coimbatore, India

ABSTRACT

The present study investigates the *in vitro* cytotoxic efficacy of polymer encapsulated bare and Mn-doped ZnO nanoparticles against human liver carcinoma Huh7 cell lines. PEG capped bare and Mn (2.0, 2.5 and 3.0 wt%) doped ZnO nanoparticles were synthesised through chemical precipitation method. The structural and morphological interpretations of the prepared nanoparticles were carried out using X-Ray Diffraction (XRD), Transmission Electron Microscopy (TEM) techniques. Optical absorption, emission properties and functional group analysis were carried out using UV-Vis, PL and FTIR techniques. The XRD results confirmed the hexagonal wurtzite crystal structure of nanoparticles with an average particle size of 17.19 nm. The anticancer ability of the prepared samples against the human liver carcinoma cell line Huh7 was investigated by studying the cell penetration, cell viability and ROS generation mechanisms.

ARTICLE HISTORY

Received 17 March 2019
Accepted 14 June 2019

KEYWORDS

ZnO nanoparticles;
anticancer activity; ROS
generation

Introduction

Nanotechnology epitomises novel and wide new technologies for both biological and biomedical engineering. The extensive interest originates from the fact that nanotechnology offers synthesis of materials with tunable properties and size less than 100 nm. These exceptionally small-sized nanomaterials are analogous to several proteins and biomolecules ingrained in the cell. It also promotes the materials to have distinctive interactions with cell biomolecule, enabling physical transport into the internal structures of cells. The materials under nano-dimension possess larger availability of surface atoms, which can lead to increased surface reactivity. By appropriate engineering design, the Gold and Iron oxide nanomaterials acquire the ability to target selectively agents for the treatment of cancer and have successfully been utilised in cancer therapy. Semiconducting nanoparticles have earned much attention since last decades, due to their unique physical and optical properties. Owing to their large surface to volume ratio, they have immense applications especially in fabricating of photo-conductive devices [1]. In addition to their inborn properties, they also have the ability to encapsulate or bind to several therapeutic agents such as proteins, hydrophobic and hydrophilic drugs, etc. Zinc oxide (ZnO) and Zinc sulphide (ZnS) belongs to group II – VI compounds and have hexagonal wurtzite structural phases in common. The wurtzite phased ZnO and ZnS nanomaterials have larger exciton binding energy due to their wider band gap (3.4 eV & 3.9 eV) and are well suited for room temperature ultraviolet

photoluminescence and piezo-electric capabilities [2]. Both ZnO and ZnS semiconducting nanomaterials are inexpensive, non-toxic and chemically balanced thus making them potential candidates in the area of gas sensors, solar cells optical and piezo-electric devices, lasers and manufacturing ferro-electric memory devices [3,4]. Zinc oxide is a favourable theranostic agent extensively used in cancer therapy compared to Zinc sulphide. This may be due to its inherent wide band gap which is useful in generating reactive oxygen species in cancer cells. In addition, certain nanoparticles have been realised to be a potential candidate for biochemical modulation and have possible future application in clinical cancer chemotherapy. Furthermore, recent in-vitro studies indicate that certain metal oxide nanoparticles can preferentially kill cancer cells, with remarkably less toxicity against normal cells [5]. Hence, considerable interest has been put forwarded in further optimising the nanoparticle specificity and anticancer properties by functionalising them with antibodies or other ligands aimed at targeting cancer molecules. Among several classes of nanomaterials, metal oxide nanostructures have gained much importance due to their interaction ability with cancer cells. ZnO is a conventional wide band-gap semiconductor with band gap of 3.2 eV and a widely discussed material. Although ZnO-based nanoparticles have been studied by multidisciplinary research community for several decades, they have limitedly been explored in cancer applications [6,7]. The ability of ROS generation by ZnO nanoparticles depends on their optical and structural properties. Though we have numerous reports on structural and optical

properties pertain to in-vitro cell killing effect, very limited level of success only has been achieved [8,9]. These limitations are influenced by so many factors, such as high concentration, low efficiency, suitable capping agents, size-controlled synthesis protocol, etc. Though nanotechnology offers extraordinary features, compatibility of nanomaterials is the only concern which has to be emphasised. Henceforth, it is essential to make them biocompatible so as to reduce its adverse side effects and improve its anti-tumour activity. Capping of nanomaterials with suitable hydrophilic group agents is a challenging process in the synthesis of biocompatible nanomaterials. Several polymers have been proposed, among them, Polyethylene glycol (PEG), Poly-vinylpyrrolidone (PVP) are commonly used polymers since they have several advantages and functions such as *in vitro* dispersion, stability, solubility, biocompatibility and most importantly to reduce toxicity [10–16]. Polyethylene glycol (PEG) is inexpensive, versatile, and FDA-approved polymer and several studies show magnetic nanoparticles with a PEG-modified surface showed appreciable increase in cellular uptake by breast cancer cell BT20 compared to un-modified particles. The increased solubilisation of the nanoparticles in the cell membrane lipid bilayer mediated by PEG, most possibly the reason for higher uptake [17,18]. Furthermore, Zinc oxide nanoparticles with suitable metal dopant such as Manganese (Mn) increases the surface defects thereby generating photo oxidation reactions which is a promising treatment in cancer therapy [19]. However, consistent analysis of PEG capping onto ZnO nanoparticles and its elevated cytotoxic nature has not been explored completely.

In our present study, we synthesised PEG-modified Mn-doped ZnO (2.0%, 2.5% & 3.0 wt %) nanoparticles and investigated the dose-dependent cytotoxic nature of the surface functionalised nanoparticles against Huh7 human liver cancer cell lines. From our observation it has been found that the 2 wt% Mn-doped ZnO nanoparticles have elevated cytotoxic effects against Huh7 cell lines compared to higher dopant concentrations. The antibacterial ability was also carried out against gram positive and gram negative bacterial organisms. Compared to undoped, the Mn-doped ZnO samples showed distinctive cytotoxic results which make them promising agents for biomedical applications.

Experimental

Chemicals

All the reagents were of analytical grade, purchased from Merck and were used without further purification. Zinc acetate dihydrate ($\text{Zn}(\text{CH}_3\text{COO})_2 \cdot 2\text{H}_2\text{O}$), Sodium bicarbonate (NaHCO_3), manganese acetate tetra hydrate ($\text{Mn}(\text{CH}_3\text{COO})_2 \cdot 4\text{H}_2\text{O}$), and Polyethylene glycol (PEG-

6000) were used to prepare PEG encapsulated pure and Mn-doped ZnO nanoparticles. Biological reagents used for the experiments with cells, such as RPMI 1640 medium, fetal bovine serum (FBS), Penicillin/streptomycin, 2,7-dichlorofluorescein diacetate (DCFH-DA, 97%), 3-(4,5-dimethylthiazol-2-yl)-2,5-diphenyltetrazolium bromide (methyl tetrazolium, MTT, 97.5%) and phosphate-buffered saline (PBS, pH 7.4) were purchased from Sigma-Aldrich.

Synthesis of PEG encapsulated pure ZnO nanoparticles

Zinc acetate dihydrate ($\text{Zn}(\text{CH}_3\text{COO})_2 \cdot 2\text{H}_2\text{O}$) (0.1 M) was dissolved in 200 ml distilled water and stirred for 30 min. Meanwhile, PEG 6000 solution was prepared by dissolving 100 mg in 20 ml distilled water and was added drop wise to the above solution. To this mixture, 0.2 M of NaHCO_3 was prepared separately and was added drop wise into the above solution under constant stirring. After being stirred at room temperature for 2–3 h, the as-formed precipitates were filtered, washed several times with ethanol and finally dried in hot air oven at 80°C to get PEG-modified ZnO nanoparticles.

Synthesis of PEG encapsulated Mn-doped ZnO nanoparticles

The manganese precursor (2 wt%) (CH_3COO)₂ Mn·2H₂O) was dissolved in 100 ml of distilled water and stirred for 2 h which forms solution A. Meanwhile 0.1 M zinc acetate dihydrate [$\text{Zn}(\text{CH}_3(\text{COO}))_2 \cdot 2\text{H}_2\text{O}$] was dissolved in 200 ml of distilled water and stirred for 30 min which forms solution B. Then solution A and B are mixed together along with NaHCO_3 (0.2 M) solution under constant stirring at 50°C for 2 h. This mixture was added drop wise into PEG 6000 solution (100 mg in 20 ml distilled water) and kept for ageing. The resulting mixture was washed with absolute ethanol and finally dried in hot air oven at 80°C to get PEG functionalised Mn-doped ZnO nanoparticles. The above procedure is repeated to get 2.5 and 3 wt% Mn-doped ZnO nanoparticles.

Antibacterial activity

The antibacterial activity of pure and Mn-doped ZnO nanoparticles were tested against Gram-positive (Staphylococcus aureus, Bacillus subtilis) and Gram-negative (Escherichia coli, Pseudomonas aeruginosa) bacteria using disc diffusion method. The inoculums for the tests were prepared in fresh nutrient broth and were standardised to that of McFarland standards. The standardised inoculums were aseptically inoculated in the plates and excess inoculum was firmly removed. The petri dishes were kept for

solidification after which the dishes were filled with the selected bacteria. Finally, the all the lids were closed and left to dry overnight. After inoculation, each petri disks were divided into four sections and 100 µg of each sample along with the standard ciprofloxacin (10 µg) were carefully added. The petri dishes were then incubated at 37°C for 24 h. The zone of inhibition was finally measured.

Cytotoxicity analysis

Cell culture

The human liver cancer cell lines (Huh7) were purchased from National Centre of Cell Science (NCCS, Pune, India). Cells were maintained in RPMI 160 culture medium containing 10% FBS and penicillin (100 U/mL) and Streptomycin (100 µg/mL) and incubated at 37°C with 5%CO₂.

MTT-assay

The anticancer activity of pure and Mn-doped ZnO nanoparticles were determined using standard MTT assay method [16]. The dose response of liver cancer cell line undoped and Mn-doped samples were analysed using the MTT assay. All the four test nanoparticles (undoped and Mn-doped ZnO nanoparticles) each with concentrations 20, 40, 60, 80 and 100 µg/ml were exposed to the liver cancer cell lines.

Cytotoxicity assessment

Cell cytotoxicity was analyzed calorimetrically using 3-(4,5-imethylthiazol-2-yl)-2,5-diphenyl tetrazolium bromide (MTT). The Huh7 cells were seeded into 24-well plates at a density of 1×10^5 cells/well and were incubated for 24 h. Pure and Mn-doped samples were suspended in RPMI1640 medium to get the final concentrations of 20, 40, 60, 80 and 100 µg/mL and then all the nanoparticle stock solutions were ultrasonicated for 30 min to reduce agglomeration. The treatment culture atmosphere was aseptically maintained for 6, 8, 48 h. Each of the four concentrations of nanoparticles (undoped and Mn-doped ZnO nanoparticles) were added to the test cells. Following the exposure of 24 h, cell viability was measured by MTT assay. MTT was dissolved in PBS at 5 mg/mL, from this 20 µL solution was added to each well cultured cells at 37°C under a humidified atmosphere with 5% CO₂ for 24 h. The medium was then removed and washed with phosphate saline solution. After this 100 µL of DMSO was added into each well to dissolve the metabolites of MTT. The viable cells were determined by the absorbance at 570 nm by microplate reader. The viability was calculated by the following formula.

$$\% \text{ of cell viability} = \left(\frac{\text{sample O.D}}{\text{Control O.D}} \right) \times 100$$

ROS generation

The level of intracellular reactive oxygen species (ROS) generated by pure and doped ZnO samples was determined using DCFH-DA, a fluorimetric assay mainly used for oxidative stress measurements [18]. This assay penetrates into the cells and produces dichlorofluorescein (DCF). During penetration, it reacts with the reactive oxygen species induced by the nanoparticle uptake by cancer cells and results in the formation of fluorescent compound. The Huh7 cancer cells were plated into a 24-well plate at a density of 1×10^5 cells/well. The cells were incubated at 37°C for 30 min with DCFH-DA working solution. After incubation, the cells were washed twice with PBS and exposed to different concentrations 20, 40, 60, 80 and 100 µg/mL of pure and Mn-doped ZnO nanoparticles for 24 h. After exposure, the fluorescence was observed at 485 nm excitation and 525 nm emission using a Perkin Elmer Victor 31,420 multilabel plate counter. The analysis was done in triplicate for accuracy.

Results and discussion

Structural analysis

X-ray diffraction patterns of undoped and Mn (2.0%, 2.5% and 3.0%) doped ZnO nanoparticles are shown in Figure 1. The characteristic peaks with high intensities corresponding to the planes (100), (002), (101) and lower intensities at (102), (110), (103) and (112) indicate that the products exhibit high-purity hexagonal ZnO wurtzite structure matches with the JCPDS File number of 36-1451. It is evident from the XRD data that there are no extra peaks due to manganese metal, other oxides or any zinc manganese phase, indicating that the as-synthesised samples are single phase suggesting that Mn element has successfully incorporated in the Zn site [20,21]. The lattice parameters are calculated and are shown in Table 1. From the values it was observed that the lattice constants of Mn-doped ZnO were slightly larger than that of undoped ZnO because the ionic radius of Mn(II) (0.83Å) is larger than that of Zn(II) (0.74Å) following Vigard's law. The length of both *a* and *c* axis expands with increasing Mn content in ZnO lattice. The expansion of the lattice constants and the slight shift of XRD peaks of different concentration of Mn-doped ZnO indicates that manganese has exactly doped into the ZnO structure. The average crystal size (*D*) was estimated using the Scherrer's formula. The crystal size of the ZnO decreases on doping 2.0% of Mn and on subsequent doping shows an increasing tendency as shown in Table 1.

It has been observed that the PEG encapsulated ZnO: Mn²⁺ nanoparticles were more intense and sharper implying a good crystalline nature of the as synthesised ZnO products. In addition, the broadening of the

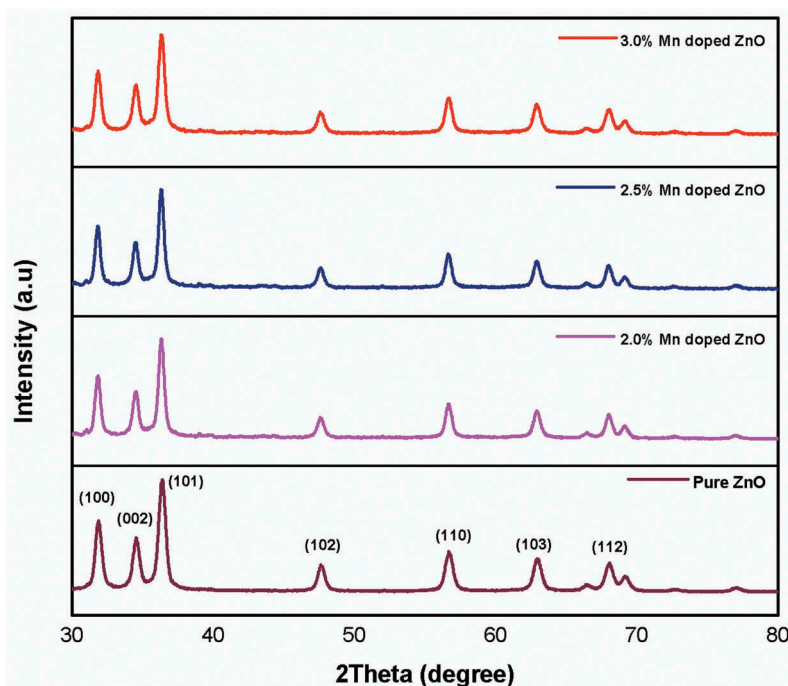


Figure 1. XRD pattern of PEG capped undoped and Mn-doped ZnO nanoparticles.

Table 1. The lattice parameters of PEG capped undoped and Mn-doped ZnO nanoparticles.

Sample	Lattice constant (Å)			Grain size D (nm)
	A	b	C	
Pure ZnO	3.248	5.204	5.204	19.11
ZnO:Mn (2.0%)	3.255	5.212	5.212	15.45
ZnO:Mn (2.5%)	3.270	5.236	5.236	17.88
ZnO:Mn (3.0%)	3.277	5.243	5.243	18.24

diffraction peaks denotes that the crystallite sizes were small as a result of Mn doping and capping of PEG. The average crystallite size of the nano-sized particles can be obtained from Debye-Scherrer formula, and the average crystallite size was found to be 17.19 nm. These results show that PEG plays an important role in controlling the ZnO particles size.

TEM analysis

Figure 2 shows the HRTEM images of PEG capped bare and Mn-doped ZnO nanoparticles. The lattice fringes of 3.0% Mn-doped ZnO a nanoparticle is shown in Figure 2(d) confirms the crystallinity of the prepared samples with interplanar distance $d = 0.244$ nm. Figure (e, f) shows the SAED pattern of the undoped and 3.0 wt% Mn-doped ZnO nanoparticles. The diffraction pattern confirms the polycrystalline nature of the samples. The diffracting planes indexed as (100), (101), (102), (110), (103) & (112) corresponds to the hexagonal phase of ZnO. From the TEM images of undoped and Mn-doped samples, the average particle size was estimated to be 20–27 nm, which is consistent with the crystallite size obtained from the XRD analysis.

Furthermore, it is also evident that the agglomeration of ZnO nanoparticles was reduced considerably. A minimal reaction time was set while preparing the PEG encapsulated ZnO nanoparticles and as a result less agglomeration was observed which might be due to the electrostatic repulsion of PEG adsorbed on the surface of the undoped and doped ZnO nanoparticles.

Uv-Vis spectroscopy analysis

The optical absorption spectra of PEG encapsulated undoped and Mn-doped ZnO nanoparticles was analyzed in the wavelength ranging from 300 to 800 nm and has been shown in Figure 3. It was observed that on increasing the dopant concentration the absorption edge shifts slightly towards lower wavelength or blue shifted indicating the enlargement of band gap [22]. This optical onset shifting can be explained by two phenomenons: (i) From the earlier reported studies, it was shown that the band gap of MnO is 4.2 eV which is significantly larger than that of ZnO 3.2 eV. This corresponds to the band gap widening in Mn-substituted ZnO nanoparticles. (ii) Burstein-Moss Effect (BME) states that the incorporation of Mn leads to the stimulation of significant quantity of free electrons which accumulates in the conduction band leading to the enlargement of optical band gap [23]. From the aforesaid explanations, it is evident that the band gap of ZnO increases on increasing Mn concentration in ZnO lattice sites.

From the optical absorption spectra, it is seen that undoped ZnO nanoparticles exhibited a strong characteristic absorption at 371 nm. Further, the absorption edges corresponding to the Mn (2.0, 2.5 & 3.0%) doped

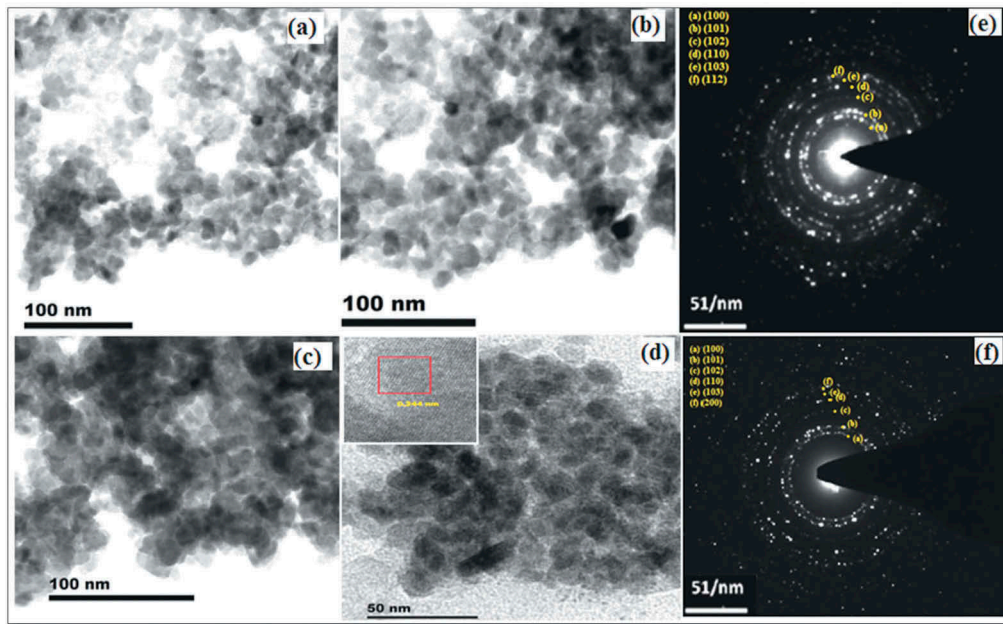


Figure 2. TEM images of (a) Pure ZnO (b) ZnO:Mn (2%) (c) ZnO:Mn (2.5%) and (d) ZnO:Mn (3%) nanoparticles, (e, f) SAED pattern of bare & Mn-doped ZnO.

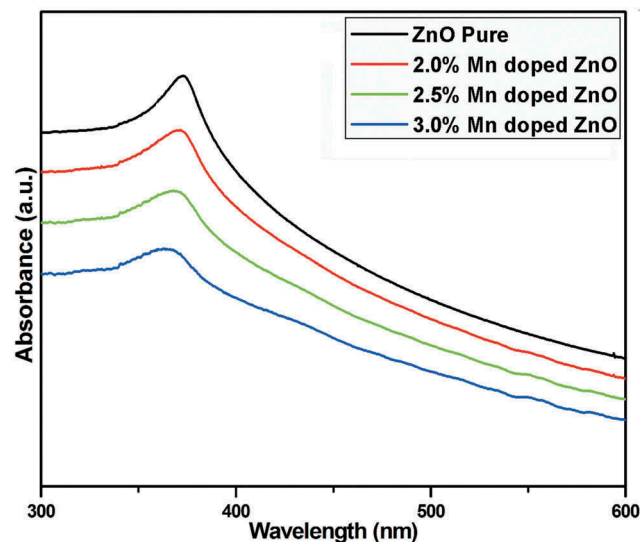


Figure 3. UV-Vis spectra of PEG capped undoped and Mn-doped ZnO nanoparticles.

ZnO nanoparticles are observed at 368, 365, and 360 nm, respectively. The band gap energy of the samples was calculated using the formula $E_{bg} = hc/\lambda$, where h is the Planck's constant (4.1357×10^{-15} eV s), c is the velocity of light ($2.997,924 \times 10^8$ m/s), and λ is the absorption wavelength (nm). The optical band gap energy of undoped and Mn-doped ZnO nanoparticles are calculated as 3.24 eV, 3.30 eV, 3.36 eV and 3.39 eV, respectively. It is seen that the band gap value of Mn-doped samples increases on increasing the dopant concentration. Furthermore, from the measured band gap value, it is seen that the absorption spectra of PEG capped undoped and Mn-doped ZnO nanoparticles exhibited blue shift which might be attributed to reduced particle

size and the interaction mechanism of PEG with the ZnO lattice sites.

FT-IR analysis

For the detection of various functional groups participating in the formation of PEG capped undoped and Mn-doped ZnO nanoparticles, FTIR measurement was carried out in the region 400 to 4000 cm^{-1} and shown in Figure 4.

The narrow absorption peak at around 1428 cm^{-1} corresponds to the bending vibration of methylene group. The band observed at around 1102 cm^{-1} is assigned to the typical C-O-C vibrations of the capping

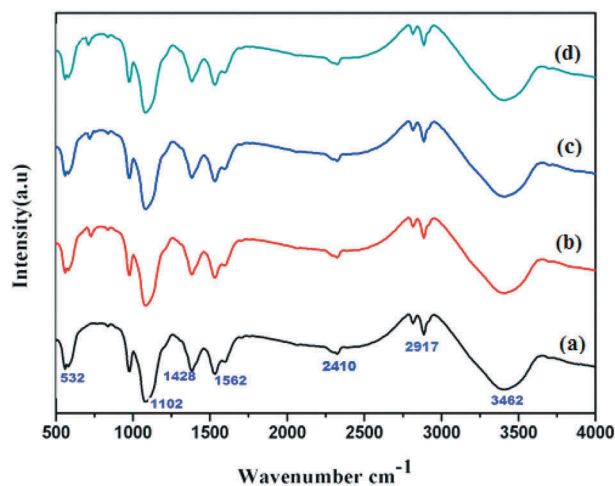


Figure 4. FTIR spectra of (a) Pure (b) ZnO:Mn (2%) (c) ZnO:Mn (2.5%) and (d) ZnO:Mn (3%) nanoparticles.

agent PEG. The absorption peak at 2831 cm^{-1} corresponds to the CH group stretching vibration of the surfactant PEG. Furthermore, this absorption peak confirms the presence of capping agent PEG on the surface of undoped and Mn-doped ZnO samples. A broad absorption band around 3462 cm^{-1} has been assigned to the stretching vibration mode of the O-H group originated from the capping of PEG. The low-intensity absorption peak observed at 2410 cm^{-1} is attributed to CO_2 and C-H modes, respectively [24]. The bands observed at around 2841 cm^{-1} and 2917 cm^{-1} correspond to the symmetric and asymmetric vibration modes of the CH_2 group. The absorption band at 1562 cm^{-1} has been assigned to the first overtone of the central O-H stretching mode vibration. The succeeding absorption band at 1428 cm^{-1} corresponds to the asymmetric stretching vibration vs (COO^-) of the acetate species [25]. The band at 532 cm^{-1} is assigned to the stretching vibrations of Zn-O bond. A localised vibrational mode corresponding to the substitution of Mn^{2+} ions into the ZnO lattice was observed at 640 cm^{-1} for the doped samples alone. This confirms the successful incorporation of dopant into the ZnO lattice sites.

Photoluminescence analysis

The optical emission properties of the pure and Mn-doped ZnO nanoparticles were investigated by PL spectroscopy shown in Figure 5. The pure ZnO nanoparticles exhibited a strong UV emission band at 383 nm and defect bands corresponding to weak blue band near 435 nm and a weak green emission band near 490 nm. The characteristic band emerged due to the near band edge emission (NBE) of ZnO at the UV region, originated due to the recombination of free excitons through an exciton-exciton collision process [26]. The peak at around 485 nm emerges owing to the electron transition occurring from Zn interstitials to the valence band, and the peak at 435 nm might be due to the result of the singly ionised

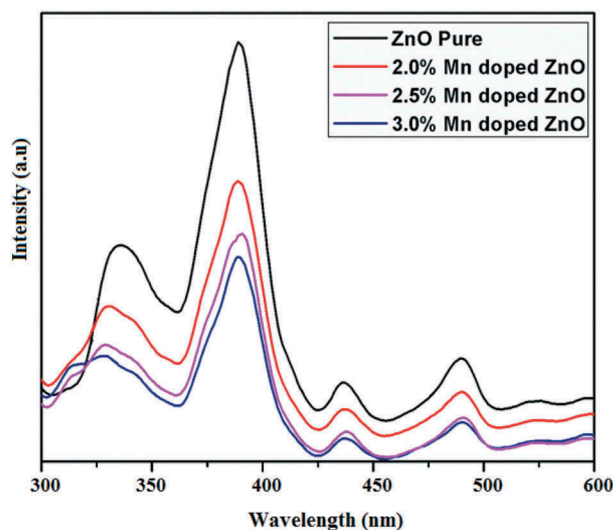


Figure 5. Photoluminescence spectra of pure and Mn-doped ZnO nanoparticles.

oxygen vacancy. The higher concentration of Mn induces higher defects density, which acts as the non-radiative recombination centres and reduces the intensity of both UV and blue emitted light.

The presence of defects density and oxygen vacancies induced due to the incorporation of Mn^{2+} ions are responsible for optical absorption and the emission spectra [27]. In addition, the occurrence of weak orange-red emission around 540–590 nm may be attributed to the presence of oxygen interstitial defects or zinc interstitial. From the PL spectra of undoped and doped ZnO nanoparticles, it can be concluded that due to incorporation of Mn^{2+} ions into the ZnO lattice sites and PEG capping, blue shift towards near band emission was observed. This blue shift phenomenon is elucidated by Burstein-Moss effect (BME) [28]. The principle states that the Fermi level of a material shifts into the conduction band by the addition of metal ions so that the transition occurs from the valence band (VB) to the top of the Fermi level directly bypassing the bottom of the conduction band (CB). This variation in the transition levels leads to the expansion of energy gap which in turn results in blue shift in the UV region.

Antibacterial activity

The antibacterial activity of undoped and Mn-doped ZnO nanoparticles were tested against Gram-positive (*Staphylococcus aureus*, *Bacillus subtilis*) and Gram-negative (*Escherichia coli*, *Pseudomonas aeruginosa*) bacteria using disc diffusion method. Ciprofloxacin ($10\text{ }\mu\text{g}/\text{disc}$) was used as the reference drug. Table 2 summarises the antibacterial activity of Mn-doped ZnO nanoparticles against all the tested organisms.

The antibacterial effect was analyzed by measuring the inhibition zones in the plates. The antibacterial efficiency

Table 2. Inhibition zone diameters of gram-positive and gram-negative bacteria against pure and Mn-doped ZnO nanoparticles.

Organisms		Zone of inhibition (mm)				
		Control	Samples			
			Pure ZnO	2% Mn	2.5% Mn	3.0% Mn
Gram positive	Staphylococcus aureus	28	18	20	23	26
	Bacillus subtilis	29	18	20	22	25
Gram negative	Escherichia coli	40	25	27	28	32
	Pseudomonas aeruginosa	41	21	23	25	28

of ZnO nanoparticles is ascribed to the reactive oxygen species (ROS) generation on the surface of the test organisms, release of Zn^{2+} ions into the bacterial medium which in turn penetrates into cell membrane causing cell death [29,30]. Figure 6 shows the antibacterial activity of undoped and Mn-doped ZnO nanoparticles on both gram-positive and gram-negative bacteria. It was observed that the Mn substituted ZnO nanoparticles exhibited remarkable and well extended inhibition zones around the samples.

Moreover, the zone of inhibition for all the four bacteria increases upon increasing the dopant concentration. The widening of inhibition zone is due to the incorporation of Mn ions into the Zn sites, causing ROS generation which in turn ruptures the cell membrane resulting in bacterial cell death. On comparing the antibacterial activity of undoped and Mn-doped ZnO nanoparticles against gram-positive and gram-negative bacteria, the killing effect is relatively higher in gram negative bacteria (Escherichia coli, Pseudomonas aeruginosa). This difference may be due to the unique interaction mechanism of ZnO nanoparticles with the bacterial membrane. Gram-positive bacteria contains thick layer of peptidoglycan and teichoic acid on the plasma membrane. Gram-negative bacteria contains relatively thin layer of peptidoglycan capped with

negatively charged lipopolysaccharides. Hence, the Zn^{2+} ions liberated by the incorporation of Mn into ZnO nanoparticle readily binds with the negatively charged polysaccharide groups leading to rapid cell death [31]. Therefore, the killing effect of undoped and Mn-doped nanoparticle is higher in gram negative bacteria compared to that of gram positive bacteria.

Cytotoxicity analysis

Cell penetration

Cell penetration capabilities of different dosage levels (20, 40, 60, 80 & 100 $\mu\text{g/mL}$) of undoped and Mn-doped ZnO nanoparticles were tested against the human liver cancer cell lines Huh7 for a total culture period of 3 h. The obtained results revealed that 100 $\mu\text{g/mL}$ dosage concentration of each of the four nanoparticles showed strong cell penetration activity shown in Figure 7.

The accelerated and unbounded growth of cancer cell makes them establish weak intracellular network forces between their cells [32,33]. Due to this weak force, the lymphatic system of the cancer cells is not properly developed and has pores ranging from micro to several nanometers (approximately 50 to 100 nm). The metal oxide nanoparticle target these weak spots of cancer cells and readily diffuses through the micro pores of the blood vessels resulting in the enhanced cell penetration activity. As the cancer cell has partially grown lymph system, the diffused nanoparticle remains in the cancer cells for an adequate period of time enabling them to interact with the cells accordingly [34]. At zero culture time, no trace of any of the four nanoparticles was seen inside the cells. However, after 2 h, significant amount of nanoparticles penetrated into the cells which can be confirmed by induced apoptosis clearly indicated by the phase contrast micrographic images shown in Figure 7. Among the three dopant concentrations (2.0, 2.5 and 3.0 wt% of Mn) 2.0% Mn-doped ZnO nanoparticles with a dose level of 100 $\mu\text{g/mL}$ exhibited higher cell killing activity. The effective concentration corresponding to 50% cell viability (EC_{50}) was used to compare the quantitative cytotoxic nature of all the four prepared nanoparticles. No further cell penetration activity was observed after the total culture period of 3 h.

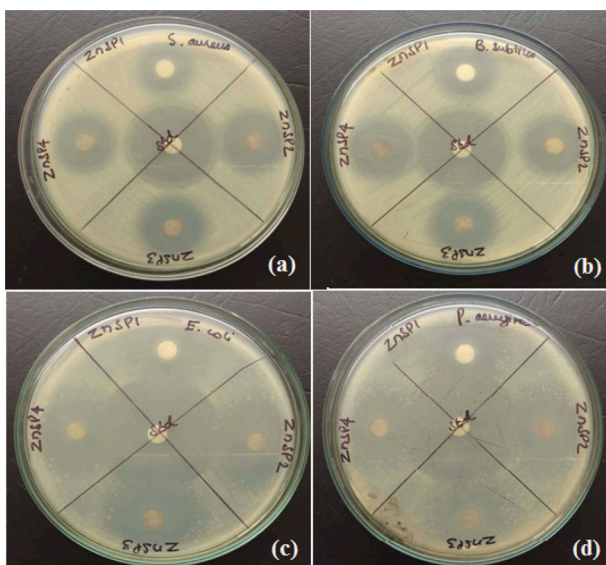


Figure 6. Gram-positive and Gram-negative bacterial inhibition zones of undoped and Mn-doped ZnO nanoparticles.

Sample codes in Figure: Znsp1 – pure ZnO; Znsp2 – 2.0% Mn-doped ZnO; Znsp3 – 2.5% Mn-doped ZnO; Znsp4 – 3.0% Mn-doped ZnO.

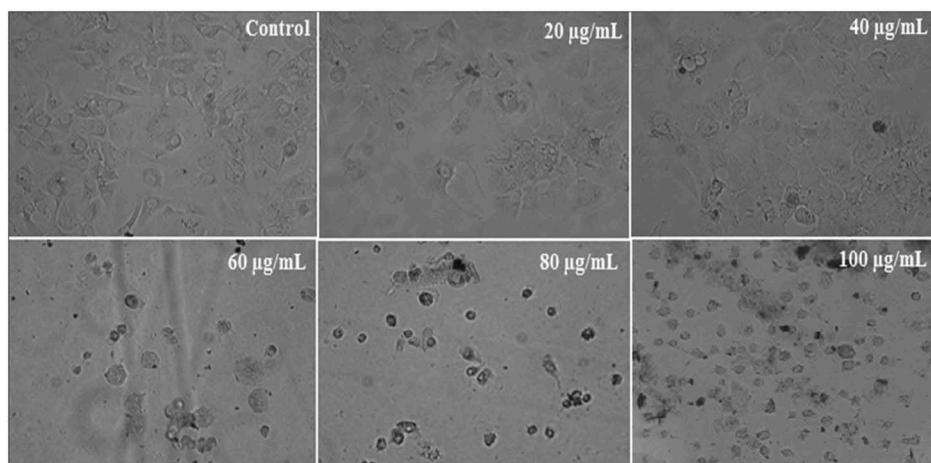


Figure 7. Phase contrast micrographs showing the induced cytotoxicity of 2.0% Mn-doped ZnO nanoparticles on Huh7 cells.

Cell viability

Five dosage concentrations (20, 40, 60, 80 and 100 µg/mL) of each of the four (undoped, 2.0, 2.5 & 3.0% Mn-doped) nanoparticles were chosen to investigate the cell viability of Huh7 cancer cells at 24 h of incubation using MTT assay. No visible cell death was observed for the undoped ZnO nanoparticles. This may be due to the multidrug resistivity of the Huh7 cancer cell membranes. At lower dosage concentration (20 µg/mL), all the four nanoparticles showed higher cell viability percentage which was shown in Figure 8. On increasing the dosage levels, significant cellular activity (mitochondrial reductase) was observed [35,36].

Zn²⁺ at a low concentration is essential for maintaining the cellular metabolism; however, higher concentration of Zn²⁺ can cause cellular toxicity. Upon increasing the dosage concentration further, the cell viability percentage of all the four nanoparticles decreased [37]. The cell viability of pure and doped ZnO nanoparticle depends on the amount of free radicals induced by each of the four dosage levels. ZnO nanoparticle readily donates free electron which readily combines with oxygen from the environment

resulting in the formation of superoxide radical anion. On the other hand, the hole generated by the donation of a free electron combines with water molecule leading to the formation of hydroxyl radicals. The generation of these free radicals increases on increasing the dosage levels of the four nanoparticles. As the nuclear cell pore of cancer cells (≈40 nm) is relatively smaller than that of ZnO nanoparticles, these free radicals get agglomerated around the nucleus which on later times damage the nucleus of the cancer cells. Our results were in consistent with the research work reported by Chuang et al. [38,39] which highlights the time and dose-dependent cytotoxic nature of ZnO nanoparticles against the human coronary artery endothelial cells. Amongst, 2.0% Mn-doped ZnO nanoparticles has the least EC-50 value for 100 µg/mL of dosage having 46.25% viable cells. On the other hand, 2.5% and 3.0% Mn-doped ZnO nanoparticles did not show visible or enhanced the cell killing activity. From this cytotoxicity result, it is proposed that 2.0% Mn-doped ZnO nanoparticles play the dominant role in killing Huh7 liver cancer cells compared to other Mn concentrations.

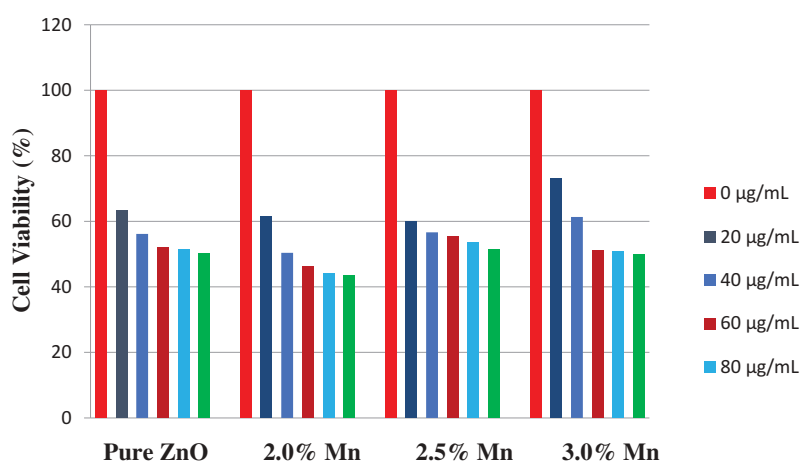


Figure 8. Cell viability percentages of pure and Mn-doped nanoparticles on human liver cancer Huh7 cells exposed for 24 h using MTT assay.

Nanoparticle-induced ROS generation

The intracellular oxidant production ability of the undoped and Mn-doped samples in liver cancer cells (Huh7) was analyzed by using the fluorescence assay DCFH-DA (2,7-dichlorofluorescein diacetate) which measures the quantity of induced hydroxyl radicals [40]. Based on our previous cell viability and penetration studies, the optimised and selected 2.0% Mn-doped ZnO nanoparticle was chosen and the dose and time-dependent ROS generation was analyzed for this concentration alone. The DCFH-DA molecules passively penetrate into the cancer cells. Inside the cancer cells, the DCFH-DA is sliced into a non-fluorescent compound, dichlorofluorescein (DCFH) by intracellular esterases and further oxidised by hydroxyl groups to a highly fluorescent molecule DCF. Thus it can be said that a unique cellular uptake mechanism plays the major role in exporting pure and Mn-doped nanoparticles into the Huh7 cells. Figure 9 shows the dose-dependent ROS generation induced by 2.0% Mn-doped ZnO nanoparticles in Huh7 cancer cells. From the fluorescence microscopy results, it is evident that the percentage of ROS starts increasing for higher concentration of the samples in the medium, which can be confirmed by the rise in fluorescence intensity. Highest percentage of ROS generation was observed for the dosage level of 100 $\mu\text{g}/\text{mL}$ with an exposure period of 24 h. Figure 10 shows the cumulative time-dependent ROS generation percentage of pure and 2.0 wt% Mn-doped nanoparticles in Huh7 cells. Upon increasing the exposure time (24 h), significant rise in ROS formation was observed.

Moreover, the ROS generation was increased with different dosage concentrations (20, 40, 60, 80 and 100 $\mu\text{g}/\text{mL}$) of PEG encapsulated 2.0% Mn-doped ZnO nanoparticles. Rapid and over production of ROS leads to cellular oxidative stress, which is the primary mechanism of nanoparticle-induced cell death [41].

Metal oxide nanoparticles significantly alter the oxidant generation process and consequently deplete the antioxidant peptide within the cell [42,43]. Based on the

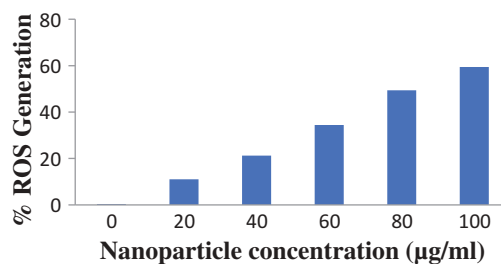


Figure 10. Dose-dependent ROS generation of 2.0% Mn-doped ZnO nanoparticles in Huh7 cell lines for a time period of 24 h.

results of the similar work done by Yip et al. it can be understood that the anticancer mechanism of pure and Mn-doped ZnO nanoparticles has several stages. Few among them are rapid production of intracellular ROS and membrane LPO in cancer cells in addition to the reduction of antioxidants in the cells. From our study, it can be suggested that oxidative stress and ROS generation play the key role in the mechanism of anticancer activity of pure and Mn-doped ZnO nanoparticles against human liver Huh7 cancer cells.

Conclusion

PEG encapsulated pure and Mn-doped ZnO nanoparticles were prepared using chemical precipitation method. XRD analysis reveals that the lattice parameters increases with increasing Mn content in ZnO nanoparticles. Reduction in average crystallite size with increasing Mn content was observed and the average crystallite size was calculated to be 17.19 nm. These results show that PEG plays an important role in controlling the particles size. EDX spectra confirm the successful incorporation of Mn ions into the ZnO lattice sites. It has been identified that upon increasing the Mn dopant concentration, incorporation of Mn ions into the ZnO lattice increased subsequently. UV-Vis spectra of Mn-doped ZnO nanoparticles exhibited blue shift indicating band gap

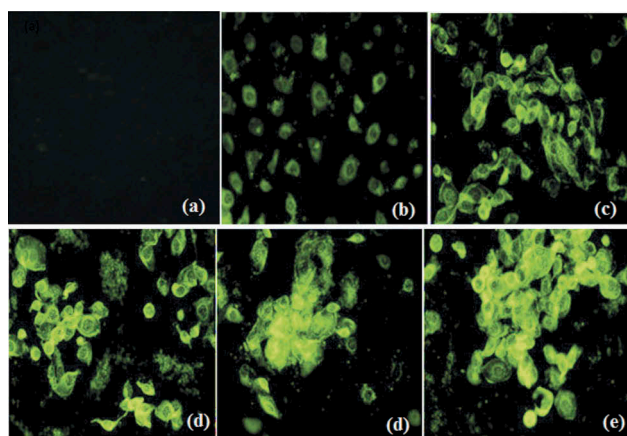


Figure 9. Dose-dependent ROS induced by (a) Control (b) 20 $\mu\text{g}/\text{mL}$ (c) 40 $\mu\text{g}/\text{mL}$ (d) 60 $\mu\text{g}/\text{mL}$ (d) 80 $\mu\text{g}/\text{mL}$ and (e) 100 $\mu\text{g}/\text{mL}$ of 2% Mn-doped ZnO nanoparticles treated for 24 h.

widening, i.e. band gap energy value of doped ZnO nanoparticles starts increasing on increasing the Mn content. Room temperature PL spectra of pure and doped ZnO samples exhibited four characteristic emission bands such as a strong UV band, weak blue and blue-green band and a weak green band indicating their structural and optical eminence. The antibacterial activity of undoped and Mn-doped ZnO nanoparticles were studied against gram positive and gram negative bacteria. The undoped and Mn-doped ZnO nanoparticles showed enhanced antibacterial activity against the gram negative bacteria (*Escherichia coli*, *Pseudomonas aeruginosa*). It was observed that the bacterial cell killing ratio started increasing for higher Mn concentrations owing to the thin layer of bacterial lipopolysaccharide layer, higher carrier concentration, reduced crystalline size and grain size.

Dose cytotoxicity of PEG encapsulated pure and Mn-doped ZnO nanoparticles were tested against human liver cancer cells (Huh7). Cytotoxicity mechanisms such as Cell viability, nanoparticle cell penetration rate and ROS generation were studied. Compared to undoped the Mn-doped ZnO nanoparticles showed higher cell killing effect which may be attributed to the combined effect of Zn^{2+} ion release and intracellular ROS generation. Thus, apoptosis induced by oxidative stress and ROS generation can be considered the possible routes of nanoparticle-induced cytotoxicity. The best cell killing results were obtained with lowest (2.0%) Mn doping concentrations. Higher Mn concentrations (2.5% and 3.0%) did not show significant cell killing activity. Thus, based on our results, it is proposed that 2.0% Mn-doped ZnO nanoparticles play the dominant role in killing Huh7 cancer cells compared to other Mn-doped ZnO nanoparticles. Our results can substantiate future cytotoxicity studies with even low concentrated Mn substitution into the ZnO sites.

Disclosure statement

No potential conflict of interest was reported by the authors.

References

- [1] Bruchez M, Moronne M, Gin P, et al. Semiconductor nanocrystals as fluorescent biological labels. *Science*. 1998;281:2013–2016.
- [2] Wang ZL, Song J. Piezoelectric nanogenerators based on zinc oxide nanowire arrays. *Science*. 2006;312:242–246.
- [3] Thiagarajan P, Kottaisamy M, Ramachandra Rao MS. SrS:Ce/ZnS:Mn – a diband phosphor for near-UV and blue- LED converted white light emitting diodes. *Luminescence*. 2009;129:991.
- [4] Ozgur U, Hofstetter D, Morko H. ZnO devices and applications: a review of current status and future prospects. *Proc IEEE*. 2010;98:1255.
- [5] Bouattour M, Payancé A, Wassermann J. Evaluation of antiangiogenic efficacy in advanced hepatocellular carcinoma: biomarkers and functional imaging. *World J Hepatol*. 2015;7:2245–2263.
- [6] Sharma V, Shukla RK, Saxena N, et al. DNA damaging potential of zinc oxide nanoparticles in human epidermal cells. *Toxicol Lett*. 2009;185:211–218.
- [7] Setyawati MI, Tay CY, Leong DT. Effect of zinc oxide nanomaterials-induced oxidative stress on the p53 pathway. *Biomaterials*. 2013;34:10133–10142.
- [8] Zhao XS, Wang ST, Wu Y, et al. Acute ZnO nanoparticles exposure induces developmental toxicity, oxidative stress and DNA damage in embryo-larval zebrafish. *Aquatic Toxicol*. 2013;136:49–59.
- [9] Zhang L, Jiang Y, Ding Y, et al. Investigation into the antibacterial behaviour of suspensions of ZnO nanoparticles (ZnO nanofluids). *J Nanopart Res*. 2007;9:479–489.
- [10] Wahab R, Mishra A, Yun SI, et al. Antibacterial activity of ZnO nanoparticles prepared via non-hydrolytic solution route. *Appl Microbiol Biotechnol*. 2010;87:1917–1925.
- [11] Durán N, Seabra AB. Metallic oxide nanoparticles: state of the art in biogenic syntheses and their mechanisms. *Appl Microbiol Biotechnol*. 2012;95:275–288.
- [12] Seabra AB, Haddad PS, Duran N. Biogenic synthesis of nanostructured iron compounds: applications and perspectives. *IET Nanobiotechnol*. 2013;7:90–99.
- [13] Rubilar O, Rai M, Tortella G, et al. Biogenic nanoparticles: copper, copper oxides, copper sulfides, complex copper nanostructures and their applications. *Biotechnol Lett*. 2013;35:1365–1375.
- [14] Rai M, Kon K, Ingle A, et al. Broad-spectrum bioactivities of silver nanoparticles: the emerging trends and future prospects. *Appl Microbiol Biotechnol*. 2014;98:1951–1961.
- [15] Rai M, Birla S, Gupta I, et al. Diversity in synthesis and bioactivity of inorganic nanoparticles: progress and pitfalls. *Nanotechnol Rev*. 2014;3:281–309.
- [16] Ingale AG, Chaudhari AN. Biogenic synthesis of nanoparticles and potential applications: an eco-friendly approach. *J Nanomed Nanotechnol*. 2013;4:1–7.
- [17] Zhang Y, Kohler N, Zhang M. Surface modification of superparamagnetic magnetite nanoparticles and their intracellular uptake. *Biomaterials*. 2002;23:1553–1561.
- [18] Yamazaki M, Ito T. Deformation and instability in membrane structure of phospholipid vesicles caused by osmophobic association: mechanical stress model for the mechanism of poly(ethylene glycol)-induced membrane fusion. *Biochemistry*. 1990;29:1309–1314.
- [19] Bhargava R, Gallagher D, Hong X, et al. Optical properties of manganese-doped nanocrystals of ZnS. *Phys Rev Lett*. 1994 Jan;72(3):416–419.
- [20] Sudha M, Senthilkumar S, Hariharan R, et al. Optical properties of manganese-doped nanocrystals of ZnS. *J Sol-Gel Sci Technol*. 2012;61:14–22.
- [21] Harikiran L, Bhikku A, Narsimha RY. In vitro cytotoxicity of gold and silver nanorods using different human cell lines. *Lett Am J Pharm*. 2015;34:1277–1282.
- [22] Wang H, Joseph JA. Quantifying cellular oxidative stress by dichlorofluorescein assay using microplate reader. *Free Radic Biol Med*. 1999;27(5–6):612–616.
- [23] Sharma VK, Varma GD. Investigations on the effect of gaseous environment during synthesis on the magnetic properties of Mn-doped ZnO. *J Alloys Compounds*. 2008;458:523–527.

- [24] JayanthiSharda K, Chawla S, Synthesis of Mn doped ZnO nanoparticles with biocompatible capping. *Appl Surf Sci.* **2010**;256(8):2630–2635.
- [25] Phan TL, Yu SC. Optical and magnetic properties of $Zn_{1-x}Mn_xO$ nanorods grown by chemical vapor deposition. *J Phys Chem C.* **2013**;117:6443–6453.
- [26] Suwanboon S, Ratana T, Ratana W. Fabrication and properties of nanocrystalline zinc oxide thin film prepared by sol-gel method. *J Sci Technol.* **2008**;30:65–69.
- [27] Dole B, Mote V, Huse V, et al. Structural studies of Mn doped ZnO nanoparticles. *Curr.Appl.Phys.* **2011**;11:762–766.
- [28] Xie X, Shang P, Liu Z, et al. Synthesis of nanorod-shaped cobalt hydroxycarbonate and oxide with the mediation of ethylene glycol. *J PhysChem C.* **2010**;114:2116–2123.
- [29] Park WI, Yi GC, Jang HM. Structural and optical properties of $Zn_{1-x}Mg_xO$ nanocrystals obtained by low temperature method. *J Appl Phys.* **2006**;100:034315.
- [30] Manabu G, Naoko O, Kenichi O, et al., Photoluminescent and structural properties of precipitated ZnO fine particles. *Jpn J Appl Phys.* **2003**;42(2A):481–485.
- [31] Zang L, Jiang Y, Ding Y, et al. Investigation into the antibacterial behaviour of suspensions of ZnO nanoparticles. *J Nanopart Res.* **2007**;9:479.
- [32] Prashanth GK, Prashanth PA, Bora U, et al. In vitro antibacterial and cytotoxicity studies of ZnO nanopowders prepared by combustion assisted facile green synthesis. *Karbala Int J Mod Sci.* **2015**;1:67–77.
- [33] Kao YY, Chen YC, Cheng TJ, et al. Zinc oxide nanoparticles interfere with zinc ion homeostasis to cause cytotoxicity. *Toxicol.Sci.* **2011**;125:462–472.
- [34] Choi O, Hu ZQ. Size dependent and reactive oxygen species related nanosilver toxicity to nitrifying bacteria. *Environ Sci Technol.* **2008**;42:4583–4588.
- [35] Bacchetta R, Moschini E, Santo N, et al. Evidence and uptake routes for Zinc oxide nanoparticles through the gastrointestinal barrier in *Xenopus laevis*. *Nanotoxicology.* **2014**;7:728–744.
- [36] Bahsi ZB, Oral AY. Effects of Ag-induced acceptor defects on the band gap tuning and conductivity of Li: ZnO films. *Opt Mater.* **2007**;29:672.
- [37] Dhanalakshmi A, Natarajan B, Ramadas V, et al. Structural, morphological, optical and antibacterial activity of rod-shaped zinc oxide and manganese-doped zinc oxide nanoparticles. *Pramana J Phys.* **2016**;87:57.
- [38] Wahab R, Siddiqui MA, Saquib Q, et al. ZnO nanoparticles induced oxidative stress and apoptosis in HepG2 and MCF-7 cancer cells and their antibacterial activity. *Colloids Surf B.* **2014**;117:267–276.
- [39] Wang C, Hu X, Gao Y, et al. ZnO nanoparticles treatment induces apoptosis by increasing intracellular ROS levels in LTP-a-2 cells. *Biomed Res Int.* **2015**;2015:423287.
- [40] Chuang KJ, Lee KY, Pan CH, et al. Effects of zinc oxide nanoparticles on human coronary artery endothelial cells. *Food Chem Toxicol.* **2016**;93:138–144.
- [41] Iavicoli I, Calabrese EJ, Nascarella MA. Exposure to nanoparticles and hormesis. *Dose-Response.* **2010**;8:501–517.
- [42] Nel A, Xia T, Madler L, et al. Toxic potential of materials at the nanolevel. *Science.* **2006**;311:622–627.
- [43] Yip NC, Fombon IS, Liu P, et al. Disulfiram modulated ROS-MAPK and NF κ B pathways and targeted breast cancer cells with cancer stem cell-like properties. *Br J Cancer.* **2011**;104:1564–1574.